Journal of
Microscopy

Journal of Microscopy, Vol. 00, Issue 0 2017, pp. 1–17
Received 30 November 2016; accepted 20 February 2017

doi: 10.1111/jmi.12558

Enhanced spatial resolution in vector potential photoelectron microscopy

R. BROWNING
R. Browning Consultants, Shoreham, New York, U.S.A.

Key words. Materials microanalysis, photoelectron microscopy, VPPEM.

Summary

The spatial resolution of the vector potential photoelectron microscope is determined by the maximum size of the cyclotron orbits of the imaged electrons at the surface of a sample. It is straightforward to calculate the spatial resolution for any imaged electron energy given the magnetic field strength. However, in low-energy secondary photoelectron images from an aluminium–calcium metal matrix alloy, we find the apparent spatial resolution is significantly higher than expected. A possible explanation for the enhanced resolution is that the low-energy cyclotron orbits are distorted when passing from one area of work function to another and the image is dependent on the surface field distribution.

Introduction

Vector potential photoelectron microscopy (VPPEM) is a new method being developed for the chemical analysis of the surface and near surface of advanced materials at the mesoscopic scale (10–100 nm). The microscope is a full field imaging technique used with a monochromatic synchrotron x-ray light source illuminating a sample to produce photoelectrons. VPPEM images rely on the secondary electron contrast produced when x-ray photons are swept in energy across an atomic core absorption edge. This contrast gives information about the elemental distribution and the chemical state of the atoms (Stohr, 1992).

VPPEM has attributes that are expected to be valuable in the analysis of many real-world technical materials. VPPEM has a very high depth of focus and topographical effects or sample conditions have relatively little effect compared to the electrostatic cathode photoelectron emission microscopies (PEEM; Nepijko *et al.*, 2000). VPPEM also has a high detection efficiency and the information depth can be varied by changing the x-ray energy (100–10 keV).

Correspondence to: Raymond Browning, Raymond Browning Consultants, 1 Barnhart Place, Shoreham, NY 11786, U.S.A. Tel: +1 631 821 3418; e-mail: ray@rbrowning.net

VPPEM is still in development for the National Institute of Standards and Technology (NIST) at the National Synchrotron Light Source II (NSLS II) at Brookhaven National Laboratory. The ultimate spatial resolution with an upgraded instrument was expected to be 100–200 nm. This resolution is not as high as can be achieved with scanning Auger microscopy (10 nm; Martinez *et al.*, 2013), PEEM (20–50 nm; Bauer, 2012; Neff *et al.*, 2014) or the scanning X-ray probe (20–100 nm; Horiba *et al.*, 2011). However, this paper presents the results from measurements of the VPPEM analytical spatial resolution, which appear to be much higher than the calculated estimate.

The calculated VPPEM spatial resolution depends on the cyclotron radius of the photoelectrons at the sample. The cyclotron radius at the sample is determined by the magnetic field and the imaged electron energy. A good approximation for the 20–80% edge spatial resolution ρ in micrometres is

$$\rho = 3\frac{\sqrt{E}}{B} \quad (1)$$

where E is the electron energy in electron volts and B the magnetic field in Tesla (Browning, 2014a).

Figure 1 shows a VPPEM image of a 42.3 μm (line/spacing) Cu grid on top of a 12.7 μm Ni grid. This image was obtained using the prototype NIST VPPEM with a 1.8 T magnet. This image used the zero-order (white light) illumination from beamline U4A at the National Synchrotron Light Source (NSLS), and was imaged with 1.0 eV electrons. The maximum cyclotron orbit radius will be 1.87 μm and from Eq. (1), a 20–80% edge spatial resolution of 1.7 μm. The 20–80% edge resolution measured across the shadowed grid edges is 1.8 ± 0.1 μm in agreement with calculations. Note that 15–20 T magnets are available for use with a future VPPEM instrument.

The beamline is at a 15° angle illuminating the sample from the top left-hand side. The imaging depth of the Figure 1 can be estimated as 33 μm from the length of Cu grid shadow.

The agreement between measured and calculated spatial resolution appears to be only part of the story. Data from an annealed Al-Ca 9% metal matrix sample previously used to demonstrate VPPEM image processing techniques

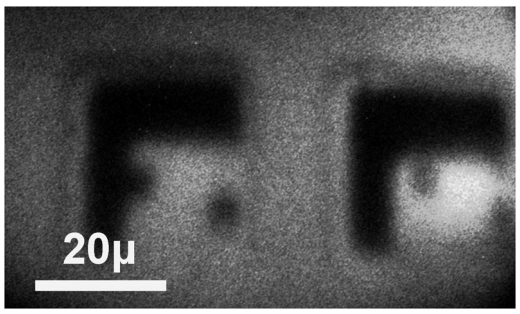

Fig. 1. VPPEM resolution test image using a 42.3 μm (line/space) Cu grid on top of a 12.7 μm Ni grid. Zero-order synchrotron light at U4A NSLS imaging 1.0 eV electrons. Measured 20–80% edge resolution 1.8 μm.

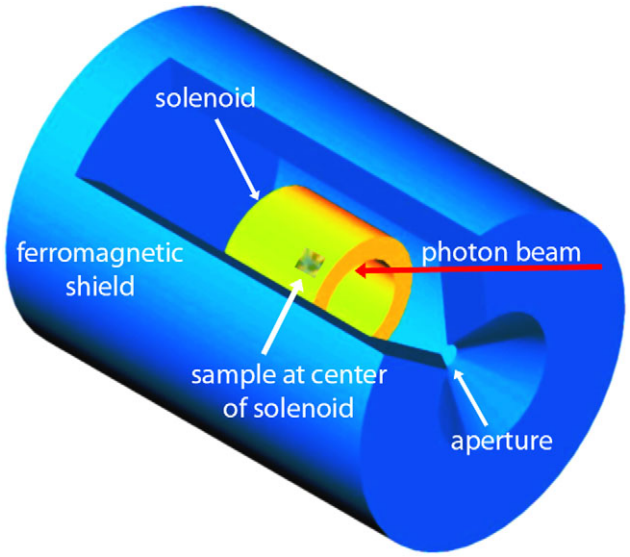

Fig. 2. Illustration of the VPPEM geometry. A cutaway of a solenoid in a ferromagnetic shield with an axial aperture. The sample sits at the centre of the solenoid and is illuminated by a photon beam.

(Browning, 2015) have been reassessed and show enhanced spatial resolution. The spatial resolution at compositional Interfaces appears to be over a factor 5 greater than expected. One possible explanation is the surface fields from chemical inhomogeneities are influencing the electron trajectories.

The VPPEM instrument

VPPEM uses a strong magnetic field around a sample to image the photoelectrons. The magnet is surrounded by a ferromagnetic shield with an aperture on the magnetic axis. The photoelectrons leaving the sample surface travel down the axis of the magnet approximately along the field lines in cyclotron orbits (adiabatic approximation). The photoelectrons then exit the field through the aperture in the ferromagnetic shield into field-free vacuum. A simplified view of the geometrical arrangement is illustrated in Figure 2.

We use the vector potential to describe the detailed action of the microscope. The vector potential $\boldsymbol{A}$ and the magnet field $\boldsymbol{B}$ are related by Maxwell's expression

$$\boldsymbol{B} = \nabla \times \boldsymbol{A} \tag{2}$$

In the uniform magnetic field at the centre of the solenoid of Figure 1, the vector potential field is radially increasing and rotating around the axis of the magnetic field in the direction of the solenoid current. The vector potential field $\mathbf{A}$ has the dimensions of momentum per unit charge. Photoelectrons from different regions on a sample will enter the vacuum with a different momentum due to the vector potential field. As the photoelectrons suddenly exit the field through the aperture, nonadiabatic conservation of the canonical momentum creates an angular image. The canonical momentum of a charged particle in a magnetic field is

$$\boldsymbol{p} = m\dot{\mathbf{r}} + q\,\mathbf{A}(\mathbf{r}) \tag{3}$$

where $\boldsymbol{p}$ is the momentum, m is the electron mass and q is the charge of the electron. This action is illustrated in Figure 3.

Figure 3 shows a set of electron trajectories which begin at equally spaced radial points just off the axis at the sample. The electron trajectories initially travel along parallel to the optical axis, and are constrained into a narrow beam by the magnetic field lines near the axis. There is a small magnification of the radial distances as the magnetic field weakens moving away from the centre of the solenoid. When the electrons exit the field through the aperture, they leave the field lines and become deflected away from the axis. The deflection produces an angular distribution dependent on the initial radial distribution at the sample. Only the radial distances are plotted in Figure 3, the electron trajectories are rotated out of the plane of the diagram.

Note that the magnetic field is not 'focusing' an image of the sample. The vector potential field provides a two-dimensional reference, which is cylindrical along the axis of the magnet. This cylindrical reference provides a large depth of field.

Spatial resolution in the VPPEM is determined by the maximum radius of the cyclotron orbits of the imaged electron at the surface of the sample. As photoelectrons are emitted at all angles, the maximum radii will be for those electrons emitted at near 90° to the surface normal. As the emitted electrons move away from the centre of the magnetic field and the magnetic field becomes weaker, the divergence of the cyclotron orbits along the field lines is a spatial magnification of the electron distribution at the surface. This effect is used in the magnetic projection electron microscope (Beamson *et al.*, 1980, 1981; Kruit & Reed, 1983; Pianetta *et al.*, 1989; King *et al.*, 1991; Fischer *et al.*, 2010). The point spread function (PSF) and the spatial resolution of the magnetic projection microscope can be calculated from the maximum electron cyclotron radius at the sample (Beamson *et al.*, 1980, 1981; Kruit & Reed, 1983). A VPPEM has the same form of spatial

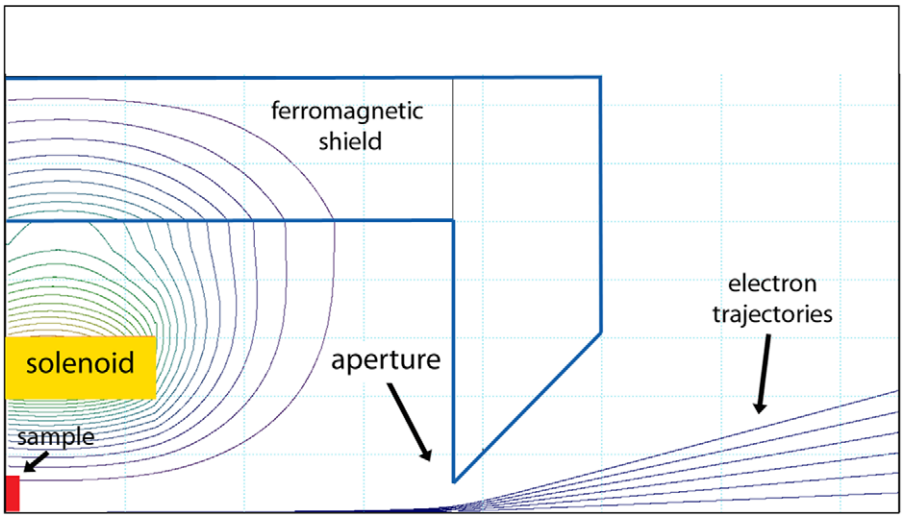

Fig. 3. Numerical simulation of the experimental geometry in Figure 2 illustrating photoelectron trajectories as they leave the sample and exit the field terminating aperture.

resolution as the magnetic projection microscope (Browning, 2014a), but because the imaged electrons are energy analyzed using a high-resolution band-pass filter outside the magnetic field, images can be made of very low-energy photoelectrons. Using low-energy electrons is advantageous for microscopy, because the spatial resolution is higher for the same magnetic field.

The overall angular divergence or the angular magnification, as the photoelectrons leave the magnetic field, can be manipulated by changing the energy of the electrons leaving the field and the size of the aperture. The electrons can also be accelerated or decelerated in the strong part of the field without distorting the image, so that the detected energy can be changed by simply biasing the sample. However, the spatial resolution is not changed.

The angular image leaving the magnetic field is energy analyzed by passing it through a concentric hemispherical analyzer (CHA) and then projecting the monochromatic angular image as a real image onto a phosphor screen. The electron optical path from the sample to the detector is illustrated in Figure 4.

The VPPEM image is created by scanning the photon energy, and collecting an image at each energy step. There is a spectrum at every pixel and this spectrum contains a wealth of information that requires analysis. As the photon energy changes, it excites different core levels in different elements. The signal that is detected is the change in intensity of the secondary electrons. Low-energy secondary electrons are created by a multistage process from a core ionization. First, an Auger electron is emitted from the photoexcited atom by ionizing a second core electron. Second, the Auger electrons lose energy, through bulk plasmon excitation, and interband transitions creating low-energy electrons. These low-energy electrons emerge as low-energy electrons into the vacuum after traversing the solid/vacuum interface. As the photon energy is changed, it gives both elemental and chemical information from the core-level energies, as well as information about the local electronic and structural environment. There is also a contribution to the secondary electron signal from the directly emitted core electron. These two signals have different information depths. The information depth of the core excitation cascade electrons can be increased up to several nanometres with high-energy x-rays (2–10 keV), whereas the mean free path of the directly emitted core photoelectron is much lower and very surface-sensitive.

Figure 5 illustrates these sources of the spectral signal in a schematic photoelectron emission energy-level diagram. In Figure 5, the vertical direction is energy and the horizontal direction represents distance out of the sample surface. Figure 5 illustrates the case of an aluminium sample with an oxidized surface. The metal is on the left and the VPPEM microscope is on the right.

The sample is irradiated by x-ray photons. If a photon, $\bar{h}\omega$, has sufficient energy, it can create a core hole in the metal by removing an electron in a core state to an empty state above the Fermi level. In the case of an insulating oxide, the core electron is removed to the conduction band edge. We expect, in theory, the Fermi level in the oxide to be midway between the conduction band edge and the top of the valence band (Kim & Brédas, 2013). The photoelectron transitions in Figure 5 are indicated by the blue vertical arrows beginning with a circle to represent the core hole remaining. Only the aluminium metal transitions have been shown. After the initial photoelectron event, the remaining core hole is filled with an electron from a higher-energy level, and this initiates an Auger cascade. The Auger cascade creates a flux of inelastically

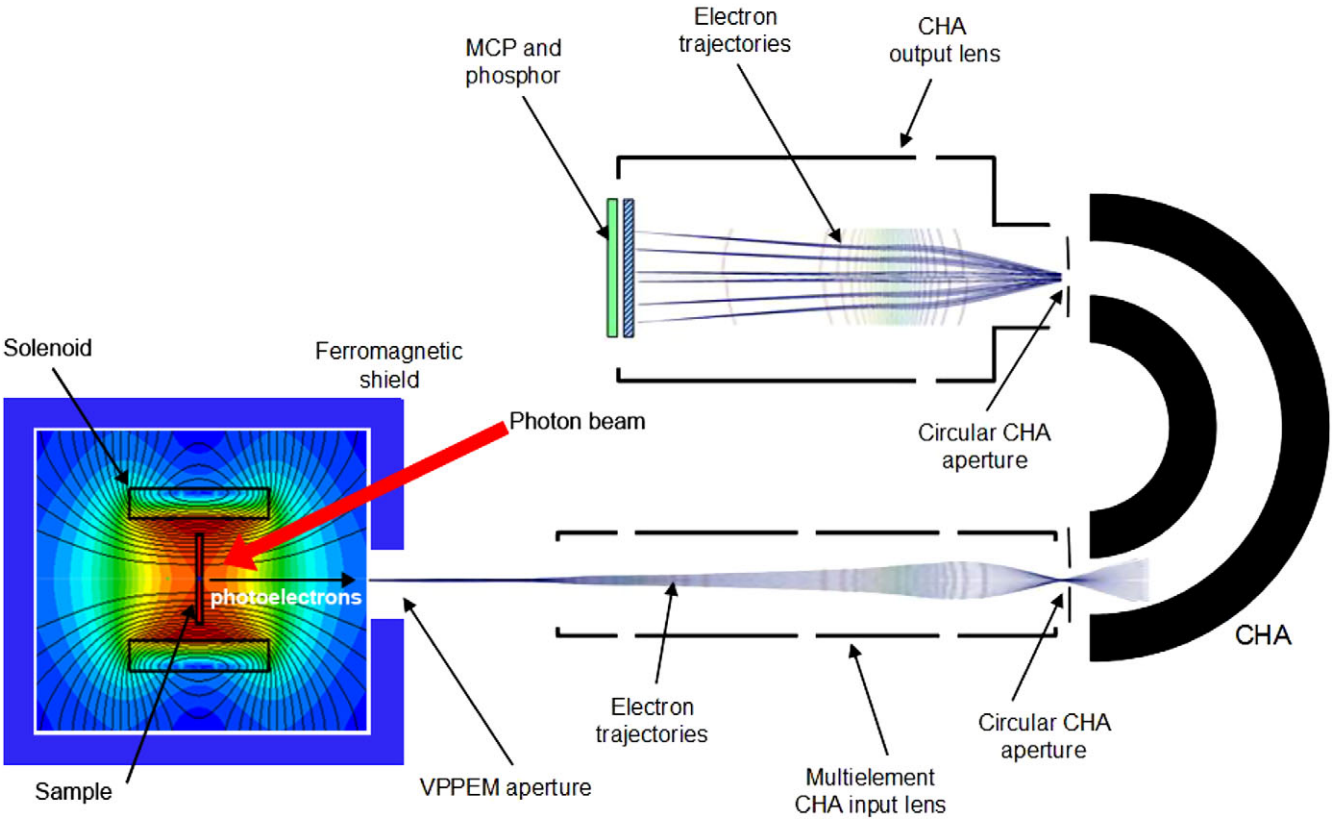

Fig. 4. Electron optical arrangement of the VPPEM. The diverging photoelectron trajectories leaving the magnetic field are focused into the aperture of a CHA. The CHA is double focusing and images a monochromatic angular image onto the output aperture. The monochromatic angular image is focused as a real image onto a multichannel plate and phosphor.

scattered electrons over a wide energy range. These electrons form the secondary electron distribution when they leave the sample. The increase in the number of secondary electrons as the photon energy is swept from a low energy up across the core absorption energy is detected by the spectrometer as a partial absorption yield near edge x-ray absorption fine structure (PAY NEXAFS) signal with a prominent feature at the core edge absorption energy.

As the photon energy is raised to several electronvolts above the core absorption energy, the directly excited photoelectron, the XPS electron, ejected from the aluminium metal core level can escape the surface directly. The directly emitted electron must have a kinetic energy above the Fermi level in the solid that is greater than the work function. An aluminium metal photoelectron also has to travel through the oxide overlayer without being absorbed. If the potential bias of the sample has been set so that the energy of the directly excited electron in the vacuum coincides with the energy window of the spectrometer, then the electron is detected. If the sample bias is fixed and the photon energy is increased, the electron energy will move through the spectrometer window to produce a peak in the spectrometer signal, the photo peak. The photo peak will be superimposed on the higher-energy part of the PAY NEXAFS structure because the core edge and the photo peak are only a few electronvolts apart (Bianconi *et al.*, 1977; Christensen *et al.*, 2011).

Experimental methods

These experiments were performed using the prototype NIST VPPEM at beamline U4A NSLS, Brookhaven National Laboratory (Browning, 2011). The NSLS facility has now been closed down and has been replaced by NSLS II. Beamline U4A was a bending magnet source with a relatively low flux density for microscopy. The U4A had three monochromators. Only the lower-energy monochromator provided sufficient photon flux for microscopy. This constraint limits the range of operation to UV photons between 15.0 and 45.0 eV, and 60.0 and 95.0 eV, and with a reduced flux in the higher-energy region. In the 60.0–95.0 eV region, the flux density is between 10^3 and 10^4 photons s^{-1} μ^{-2}. Although this flux density is many orders of magnitude lower than is typically used in photoelectron microscopy (Schmidt *et al.*, 2013), VPPEM collects 100% of the photoelectrons and the image stack is collected over a relatively long exposure time of 10–100 s. The prototype VPPEM has an approximately 100 μm diameter field of view

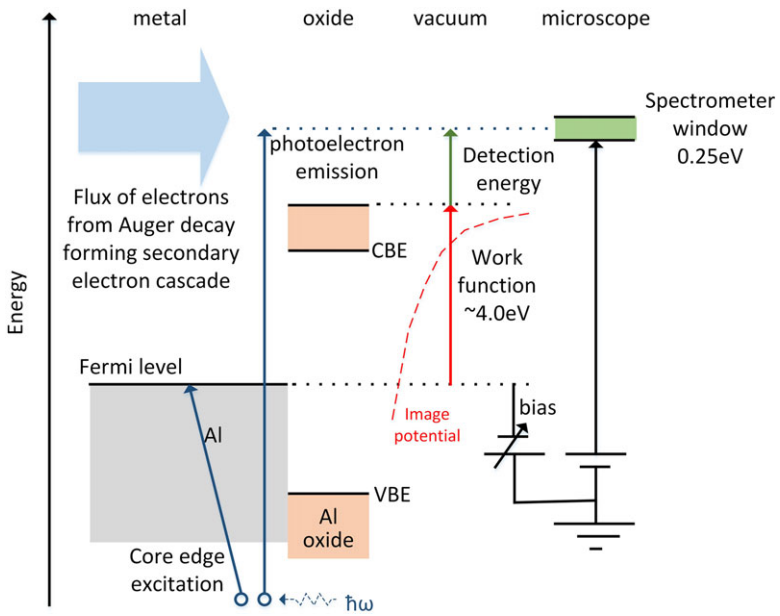

Fig. 5. Schematic energy-level diagram of the VPPEM signals from an oxidized aluminium surface.

with a depth of field of millimetres. The magnetic field and magnification are fixed in these experiments. The magnetic field is 1.8 T. The magnification is referenced to a 42.3 μm Au grid which was imaged in the same experimental sessions as the data. For the images presented here, there are 11.7 pixels μm^{-1}, 85 nm pixel size. There is a minor field distortion from nonuniformities in the iron ring used to terminate the magnetic field (Browning, 2011).

Given the constraints on the available photon energy range at beamline U4A, the choice of materials is limited. The sample used in this report was a 3 mm diameter Al-vol9%Ca metal matrix wire (Kim, 2011; Tian *et al.*, 2013). The Al 2p, Ca 3d and also the O 2s core-binding energies are within the two available energy ranges. Al-Ca metal matrix alloys have possible applications in overhead power transmission lines. Addition of calcium to aluminium alloy systems has both beneficial and deleterious effects. The alloy is lightweight and has a low electrical resistance. The metal matrix is strengthened by a high-distortion extrusion process, which forms long filaments of Ca in the aluminium. However, overheating causes intermetallics to form, embrittling the Ca filaments and reducing the strength of the alloy.

The sample has been annealed at 350°C for 4 h. Studies of the fracture surfaces show annealed specimens are coarsened with the Ca filaments nearly entirely converted to brittle intermetallics (Kim, 2011). Scanning electron microscopy (SEM) and backscatter electron images of the wire cross-section are shown in Figures 6 and 7. The cross-section is across the direction of extrusion and the SEM images are imaging the cross-sections of the long Ca filaments embedded in the Al matrix. The wire cross-section used for the SEM studies was polished with 0.05 μm diamond paste.

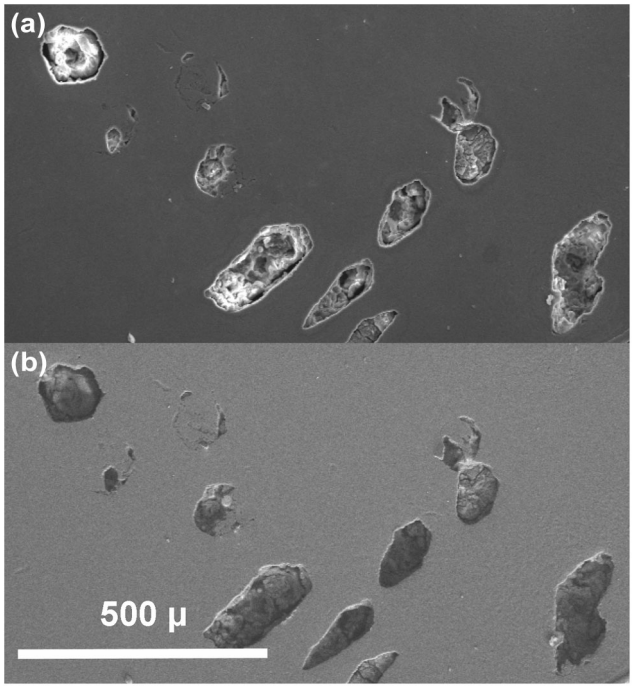

Fig. 6. (A) SEM of a polished section of an annealed Al-Ca metal matrix. (B) Backscatter electron of the area in 6(A). The Ca filaments are seen in cross-section embedded in the Al matrix.

The SEM micrographs in Figures 6 and 7 show the Ca filaments are no longer ductile and are broken with voids at the Al-Ca interface. The X-ray fluorescence indicates that the Ca has been largely consumed and the filaments are composed of intermetallics of Ca and Al (Kim, 2011). Different levels of grey

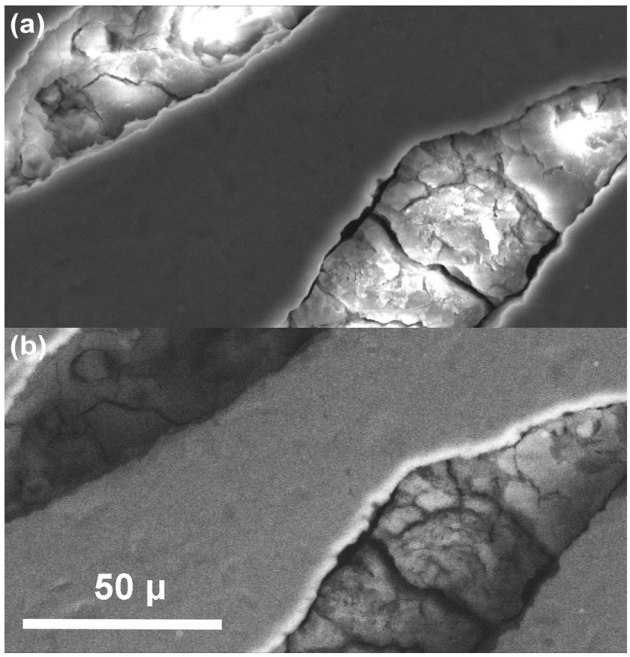

Fig. 7. A magnified view of the sample area in Figure 6. (A) SEM two Ca filaments that have formed brittle intermetallics with the Al matrix (B) backscatter electron image of the area in 7(A).

scale indicate possible changes in intermetallic composition. The bright lines around the Ca filaments are most likely SEM edge effects and are not indicative of composition.

The same specimen of Al-Ca9% wire was cross-sectioned and more coarsely polished on a 1 μm diamond grit wheel for the VPPEM studies. The sample was degreased in ethanol. The Al-Ca wire cross-section was cleaned multiple times *in situ* using an argon ion beam at approximately 45° to the face of sample surface. The ion cleaning used flowing 10^{-4} Torr argon with a turbo pump exhaust. There was sufficient contamination from background gas during ion cleaning to prevent a completely oxide-free surface being formed. The microscope main chamber was at 10^{-9} to 10^{-8} Torr. The sample surface is approximately normal to the magnetic field and the plane of the image.

VPPEM images are collected as an image stack by scanning the photon energy and collecting an image at each energy step. Part of an image stack used in this report is shown in Figure 8; the image size is 500 × 800 pixels, 42.7 μm × 68.3 μm.

The images for the image stack of Figure 8 are collected at a fixed energy in the low-energy secondary electron peak. For the prototype instrument, the legacy beam line control system could not be controlled by the image collection software. The absence of computer control required that the photon energy be set manually and the images collected individually. The photon step size was 0.5 eV, which is much coarser than typical for this type of data.

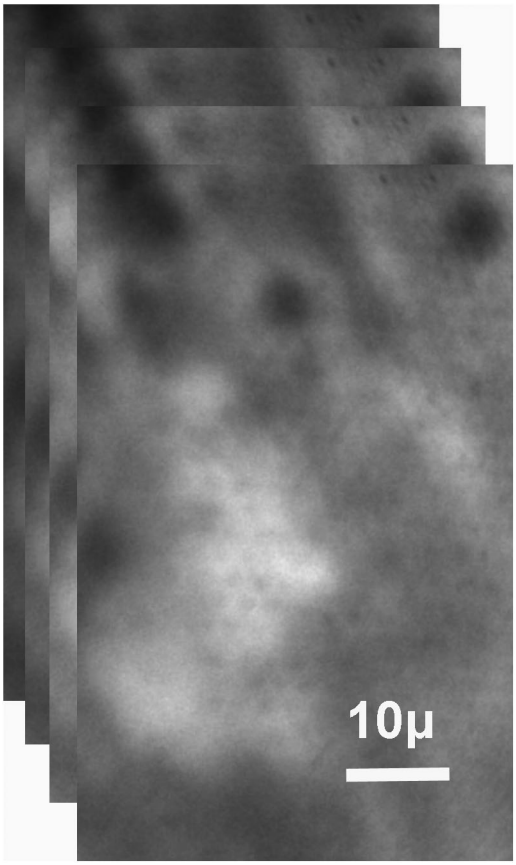

Fig. 8. Part of a VPPEM image stack showing the cross-section of a Ca filament in an annealed Al-Ca9% alloy. Higher Ca is light, higher Al is dark.

Data were collected over the two ranges of the monochromator from 20.0 to 45.0 eV which covers the Ca 3p and O 2s core features and from 70.0 to 90.0 eV which covers the Al 2p core features. The results have not been normalized against the monochromator response or synchrotron beam decay because the gold grid used for beam intensity measurement introduces gold 5p features into the Al signal. The total time to image the stack was of the order of 100 min, which includes the manual setting of the energy. The integrated exposure time at 2 s per image for 97 images was only 194 s. The long imaging time made it important to be able to align the image stack against micrometre-level instrumental drift. As can be seen from Figures 6 and 7, the sample has some strong features, which are chemistry-independent and these facilitate the alignment.

Each pixel in the image stack is a spectrum over the incident photon range. The spectra obtained from VPPEM are unusual because they contain both core edge absorption information and signal from the directly emitted photoelectrons. The sampling depth of these signals is different. This makes their detailed interpretation more difficult in light of the low spectral resolution of these experiments. Even with a simple material system, relative overlaps of the metal and surface oxide

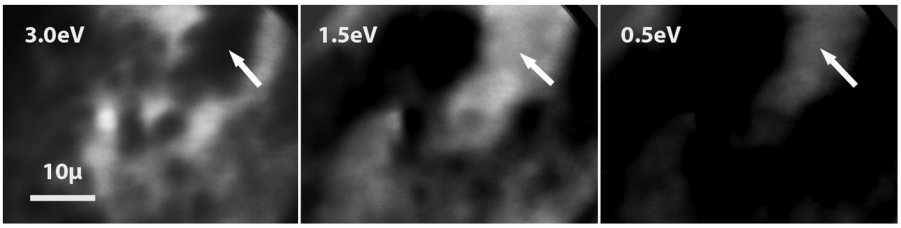

Fig. 9. A series of images of a Ca filament cross-section in an annealed Al-Ca9% alloy. The sample has been freshly ion cleaned. This series of images shows a reversal of contrast as the imaged secondary electron energy is changed. The feature indicated with an arrow is dark at 3.0 eV, bright at 1.5 eV and is becoming extinguished at 0.5 eV.

features change markedly with the energy of the electrons used for detecting the images (Browning, 2014b).

The images are typically imaged with electrons in the secondary electron peak at 1.0–2.0 eV. The true imaging electron energy depends on the source of the electrons. The surface oxides can be charged and there are work function differences across samples so that the imaged electrons at the detector are potentially at different energies as they leave the sample. The emitted low-energy electrons are accelerated to 50.0 eV for insertion into the CHA input lens (Browning, 2010). The nominal imaging energy can be changed by biasing the sample without having to change the imaging optics or the magnification. The secondary electron peak is found by changing the bias to extinguish the image signal and then plotting the image intensity against the change in sample bias. Figure 9 is a series of images with different sample bias. A range of work function can be seen in the reversal of contrast across the freshly cleaned sample. The presence of Ca-Al intermetallics might be the source of the large variations in work function on the freshly cleaned samples. There is a possible 2.0 eV difference in work function between $CaAl_4$ and Al (Uijttewaal *et al.*, 2006).

The image stack shown in Figure 8 was taken after the sample was left overnight, and shows a smaller variation in work function. The CHA energy resolution is 0.25 eV and the spectrum is sampled at 0.5 eV steps. A nominal 1.0 eV spectrum from the image stack in Figure 4 over the Al range (70.0–87.5 eV) is shown in Figure 10. This spectrum is taken from a darker region in the upper centre of the image in Figure 8.

At 74.0 eV photon energy, there is a feature due to Al 2p core-level absorption. This feature is an increase in the secondary electron yield due to a core ionization in the near surface of the Al metal followed by an Auger cascade de-exciting the core vacancy. At 78.0 eV, there is a second increase in signal due to the Al 2p core-level excitation of the aluminium oxide surface, plus a signal due to the direct emission of the Al metal 2p photoelectron. The third peak is largely from directly emitted photoelectrons with a mixture of a second oxide absorption peak. The directly emitted photoelectrons are higher in binding energy than the core transitions by the work function plus the imaging electron energy of 1.0 eV.

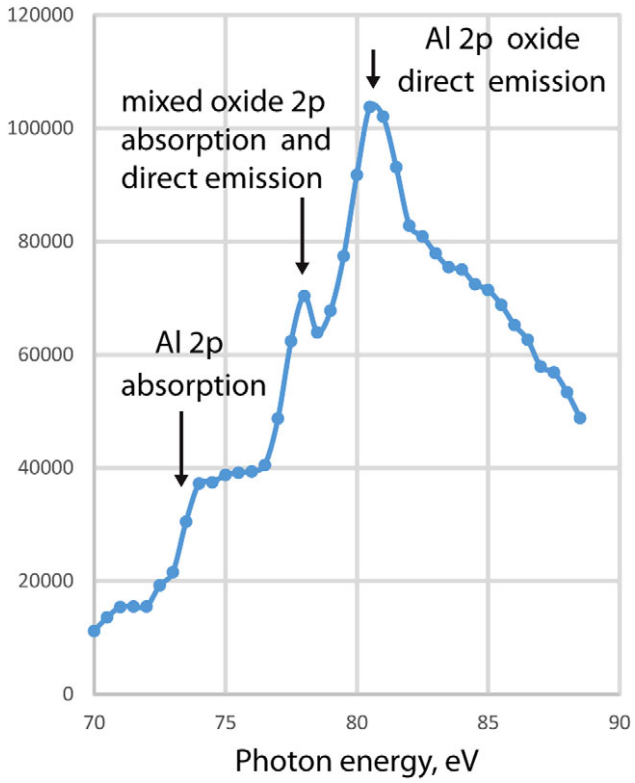

Fig. 10. VPPEM spectrum from an Al-rich region of the image stack (Fig. 8). The images are collected using 1.0 eV electrons. The Al 2p core absorption peak is at 74.0 eV. The directly emitted photoelectrons leaving the surface at 1.0 eV are 5.0 eV above the absorption energy assuming a work function near aluminium of 4.1 eV. The directly emitted electron signal overlaps with the aluminium oxide 2p absorption features.

The data shown in Figure 10 are as collected with no smoothing or background subtraction and are the summed spectra from a 1 μm × 1 μm area. The signal strengths for imaging are relatively good, with the Al 2p signal at 74.0 eV being over half the total signal. The mixed peaks can be separated and the contributions identified by changing the sample bias. This was demonstrated in a previous report (Browning, 2014b). However, much of the chemical detail (Bianconi *et al.*, 1977) is not resolved in the spectrum. The resultant images

have only elemental not chemical contrast due to the low-energy resolution of these results.

The analysis is begun by sampling 1 μm × 1 μm areas across the aligned image stack on areas of interest. The spectra of the pixels in each area are summed. From the 1 μm × 1 μm test areas, spectra with large characteristic differences can be identified. These characteristic spectra are used to create factor images. Making factor images entails creating a pixel-by-pixel root mean square estimate of the fit of the characteristic spectrum (Browning, 2015).

The value of the fit at each pixel is used to make an image. A good fit is a bright pixel and a poor fit is dark. The spectra are normalized against the sum of the intensities in the spectra

$$s'_k = \frac{n.s_k}{\sum_{k=1}^{n} s_k} \tag{4}$$

where s'_k is the normalized intensity of the spectral point k and s_k is the summed intensity of a small image window from an n deep image stack.

A factor image is constructed by taking the factor spectrum and performing a root mean square fit to the normalized spectrum of each pixel in the image. Then, the mean square error is subtracted from a fixed maximum image intensity

$$f_{x,y} = 0.95 - m\sqrt{\sum_{k=1}^{n}\left(s_{x,y,k} - s^F_{x,y,k}\right)^2} \tag{5}$$

where $f_{x,y}$ is the intensity of the factor image at pixel x, y. The signal $s_{x,y,k}$ is the intensity of the image stack at position x,y image k. The signal s^F_k is the intensity of the element k in the factor spectrum, m is a scaling factor to produce a good contrast range and 0.95 is the white level. Pixels that are highly correlated with the factor are bright. Pixels with low correlations and a high error are dark. The subsequent image can be partitioned by intensity and used to improve the factors.

Normally, two or three factor images give a reasonable outline of what is in the field of view. From these factor images, other more specific areas of interest are identified and new characteristic spectra are collected. From two-dimensional scatter diagrams of the initial factor images pixel intensities, any extremal clusters can be identified and different factor spectra generated.

In this report, just two extrema spectra have been found necessary to define factor images. Therefore, the F1 and F2 extrema spectra from any chosen area on the sample define the F1 and F2 images of that area.

Scatter diagrams are used to show the relationship between the pixel intensities of the two images F1 and F2. Clusters of intensities ($F1_{x,y}$, $F2_{x,y}$) in the scatter diagram are indicative of discrete elemental phase compositions (Browning, 1993). Measuring the peak signal positions of the clusters gives the signal separation between regions. We use scatter diagrams to provide an estimate of the spatial resolution. This method is based on the consideration that it is necessary that the pixels having a 20–80% signal between two signal levels represented in scatter diagram clusters must include those pixels that would be used to define the 20–80% signal between the two levels. These 20–80% signal-level pixels defining the spatial resolution will be at an interface between the regions represented by the clusters. Consequently, if we image only these 20–80% signal pixels, their spatial extent must define the 20–80% resolution. This method implicitly makes the assumption that the signal change between clusters is monotonic.

Because of the nature of the data, scatter diagrams are used as the primary tool to make estimates of the spatial resolution; although to support these estimates, comparisons are made between spatially filtered images having the expected spatial resolution and the data as measured. A further advantage of scatter diagrams is that an estimate of the noise is available from the size of the clusters and multidimensional data can be used to give additional clues to the nature of the interface. Clusters are an indication of real information in the image. The simple fact that there is separation between clusters and trajectories of pixels between clusters can be seen, is very good evidence of actual chemical distributions. The complexity of the scatter diagrams is an immediate indication of the complexity of the sample.

Use of scatter diagrams to define spatial resolution is not usual, the more common measurement method is to take a scan across a sharp straight edge. The spatial resolution is defined as the distance between positions with defined change in signal levels (Wolstenholme, 2008). The advantage of using the straight edge method is that noise can be averaged out along the edge and a better estimate of the instrumental spatial resolution can be made. Other methods rely on the image properties using the Fourier transform (Joy, 2002; Probst *et al.*, 2012). These methods are not successful with the data presented here.

Images are collected by a CCD camera. The CCD camera was a Peltier cooled camera providing JPEG-formatted images with 8 bits of resolution. Typically, 30–50 images are collected in an image stack. With the image processing software, the JPEG image intensities are converted into real numbers between 0.0 and 1.0. The final data arrays have a maximum of 13 bits of significance per pixel.

The electron image is detected using a microchannel plate that sits in front of a phosphor screen. The phosphor screen is imaged by the CCD camera via an optical fibre window. The collection of images has minor errors due to differences across the microchannel plate and phosphor. There are artifacts from the hexagonal stacking pattern in the optical fibre window. The JPEG format includes windowing artifacts and JPEG images are not pixel sharp due to ringing.

Image stack alignment is a critical step in extracting data (Browning, 2015). In the case of the microscope at U4A, there was significant image drift of several micrometres over the image stack collection time. This drift was mainly due to the change in ambient temperature cycling over the period of

some 30 min. There was also drift from the settling of the stage movement. There are some advantages to having some drift in the images. After the sample drift is removed by aligning the image stack, image imperfections due to defects in the detection system and JPEG artifacts are averaged out. However, if there are no strong topographic details in the field of view, then the image alignment routine tends to lock into the optical fibre window hexagonal stacking pattern. In this case, the images are first filtered using a fast Fourier transform (FFT). The FFT filter is effective even when the pattern removal is incomplete, but just below the level needed to allow the image alignment routine to work effectively.

The final alignment of the image stack is difficult to quantify and optimize. The current software uses a movie of the images and the amount of 'camera shake' observed by eye is used to tune the alignment routine.

The image processing software used for this report was created in-house using Microsoft Studio.

Results

An Al-Ca alloy was chosen for this experiment because both Al and Ca have core levels within the usable photon energy ranges of the U4A beamline. The full data set includes the lower range of 20.0–45.0 eV with 51 images in 0.5 eV steps. The lower range covers the Ca 3p 1/2, 3/2 (24.0–25.0 eV) core-level spectral signals, the directly emitted Ca 3p photoelectrons (30.0–35.0 eV) and the O 2s core levels (40.0–45.0 eV). The higher-energy range of 70.0 to 90.0 eV has 41 images with 0.5 eV steps covering the Al 2p core levels (73.0–74.0 eV), the Al 2p oxide core levels (78.0–80.0 eV) and the Al 2p directly emitted photoelectron signals (80.0–84.0 eV).

Because of the complexity of the Al-Ca samples, the analysis of the image data required a multistep process and a detailed inspection of the results. In a previously published report, the annealed Al-Ca alloy (Browning, 2015) was shown to have developed a complex phase distribution that included four Al-Ca intermetallics, oxides, impurity phases and voids, besides Al and Ca. The SEM micrographs (Figs. 6 and 7) show that the filaments are also broken and complex, with many cracks and voids, but with some regions of lower topography. In addition to the sample complexity, there will be variations across the Ca filaments from the effects of the strong topography influencing relative signal strengths, both from shadowing, and from changes in escape depth. Furthermore, the ion cleaning which is at 45° to the sample surface will not be uniform. Because both the bulk and the surface are sampled in the spectra, a multiplicity of features is expected, complicating the analysis. Nevertheless, we find that in locally smooth areas of the sample, the high-energy Al range gives a simpler scatter diagrams with a strong anticorrelation between end members. These scatter diagrams can be used to give an overall view of the compositions of the sample features and get a measure of the spatial resolution.

The lower-energy Ca range is more complex. The contrast changes across the lower-energy image stack makes the image stack alignment more difficult. It was not possible to align image stacks over both the Al and Ca ranges with the same accuracy as that within the ranges. However, taking the individual stacks and comparing the positions of voids and other features enabled alignment of the individually aligned ranges to the same positions on the sample with a sub-micrometre error.

An image from a region of high topographic contrast on a Ca filament is shown in Figure 11(A). This image is a single exposure at 82.0 eV from the middle of a 70.0 to 89.0 eV image stack covering the Al 2p features. The image was collected with a nominal imaging energy of 1.0 eV. The imaging energy is set by collecting a series of images with a different sample bias and fixing on the sample bias from the resultant secondary electron distribution. The secondary electron distribution is shown in Figure 11(B). The pixel size was measured in the same experimental session using a 42.3 μm Au grid and found to be 85 nm or 11.7 pixels μm^{-1}.

The spatial resolution can be estimated by taking a line scan across one of the edges shown in Figure 11(A). The line scan is shown in Figure 11(C). The 20–80% edge resolution is measured at 1.9 compared to the expected 1.7 μm.

The Al range 70.0–89.0 eV image data stack was aligned using a 200 × 200 pixel region in the top middle to the left of the dark band in Figure 11(A). After alignment, the image was cropped to 170 × 170 pixels (14.5 μm × 14.5 μm) in the more uniform region within the white square at the lower left-hand corner of Figure 11. The two extrema factor spectra F1 and F2 for this cropped image stack are shown in Figure 12.

The scatter diagram that shows the covariance of the intensities of the factor images F1 and F2 is shown in Figure 13(C). The scatter diagram has been rotated 45°. The factor images are highly anticorrelated and the main part of the image information in this region is contained in the horizontal green line. The histogram along the horizontal axis is shown in Figure 13(D).

The presence of several distinct regions is apparent in the clustering at the centre of the scatter diagram, and in the sharp peaks in the histogram in Figure 13(D). The main central peaks can be isolated by taking a 2 μm × 2 μm bounding box across the image area. The histograms from these 2 μm × 2 μm areas are shown in Figure 13(D) as the smaller peaks under the main histogram. The signal distribution along the histogram in Figure 13(B) can be imaged as a false colour image In Figure 14(A), the four main peaks have been imaged as cyan, yellow, green and orange, corresponding to those peaks in the histogram 13(D). The minima between the peaks in Figure 13(D) are chosen as boundaries. The other regions in Figure 14 have been arbitrarily assigned colours with the lowest Al signal (F2) imaged in red, whereas the highest Al signal (F1) is imaged in dark blue.

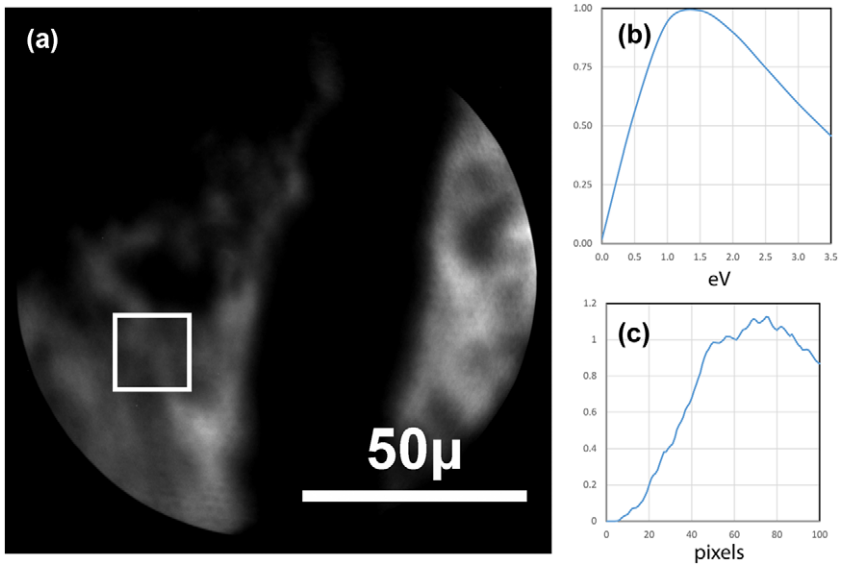

Fig. 11. (A) VPPEM image of a Ca filament with strong topography, photon energy 80.0 eV and 1.0 eV electron imaging energy. (B) Secondary electron spectrum from a Ca filament. (C) Line scan across the dark to light right edge in 11(A).

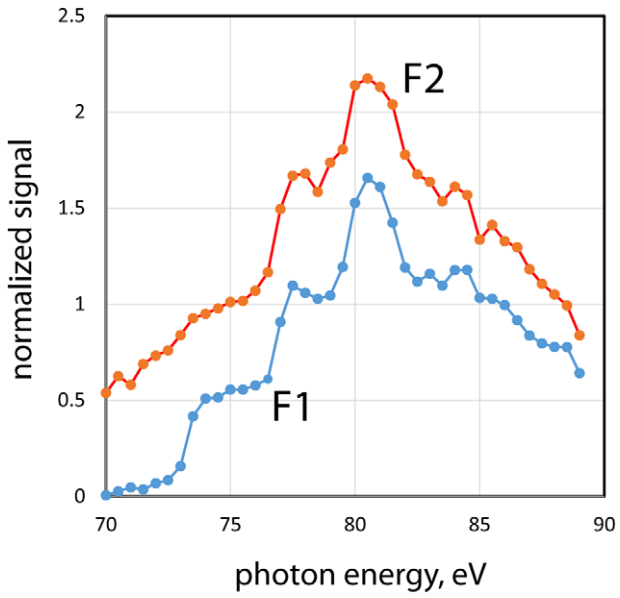

Fig. 12. Factor spectra from within the box in the lower left of Figure 11(A). F1 spectrum from an Al-rich region. The Al 2p core absorption peak is at 74.0 eV. F2 spectrum is from a region with low Al 2p core absorption.

We can get a measure of the spatial resolution by looking at the overlap between two well-defined peaks. Taking the peak positions of the peaks of the cyan and yellow regions in the histogram of Figure 13(D) and imaging the 20–80% signal overlap between regions as red pixels, gives the image in Figure 14(B). This image shows the width of the interface between the clusters. The interface is less than the expected 20 pixels. Much of the interface is 3–4 pixels wide. With 85 nm per pixel, Figure 14(B) suggests a spatial resolution in the 0.3 µm range.

The information contained in the data from the F1 and F2 images is essentially one-dimensional. We can image it directly by subtracting the F1 image from the F2 image and adjusting the contrast to fit within a 0–255 integer range for presentation in bitmap or JPEG format. This subtracted image is shown in Figure 15(A). Note that this image appears very similar to the F2 image of Figure 13(B). The image is sharper than expected. We can simulate the effect of having a 1.7 µm 20–80% edge resolution using a Gaussian blur. The resultant blurred image is shown in Figure 15(B).

These results suggest that despite the measured 1.9 µm edge resolution, much higher resolution information is directly recoverable from the VPPEM image stacks, without deconvolution.

Figure 8 shows the image stack from an area on a Ca filament with less topographic contrast compared to Figure 11. The lack of strong topographical contrast made this image stack more challenging to align. In particular, the alignment routine tended to lock onto the hexagonal stacking pattern of the optical fibre window. An FFT filter was used to reduce the effects of this hexagonal pattern.

The centre 500 × 500 pixels of the image of Figure 8 with a prominent hexagonal pattern is shown in Figure 16(A) with the FFT-filtered image in Figure 16(B). The contrast in Figures 16(A) and (B) has been increased by a factor x2 in order to bring out the pattern visually. The size of the cuts on the hexagonal pattern in frequency space was kept to a minimum and the hexagonal pattern can still be observed in Figure 16(B). However, the reduction in amplitude was sufficient to unlock the image shifting algorithm, and this then reduces

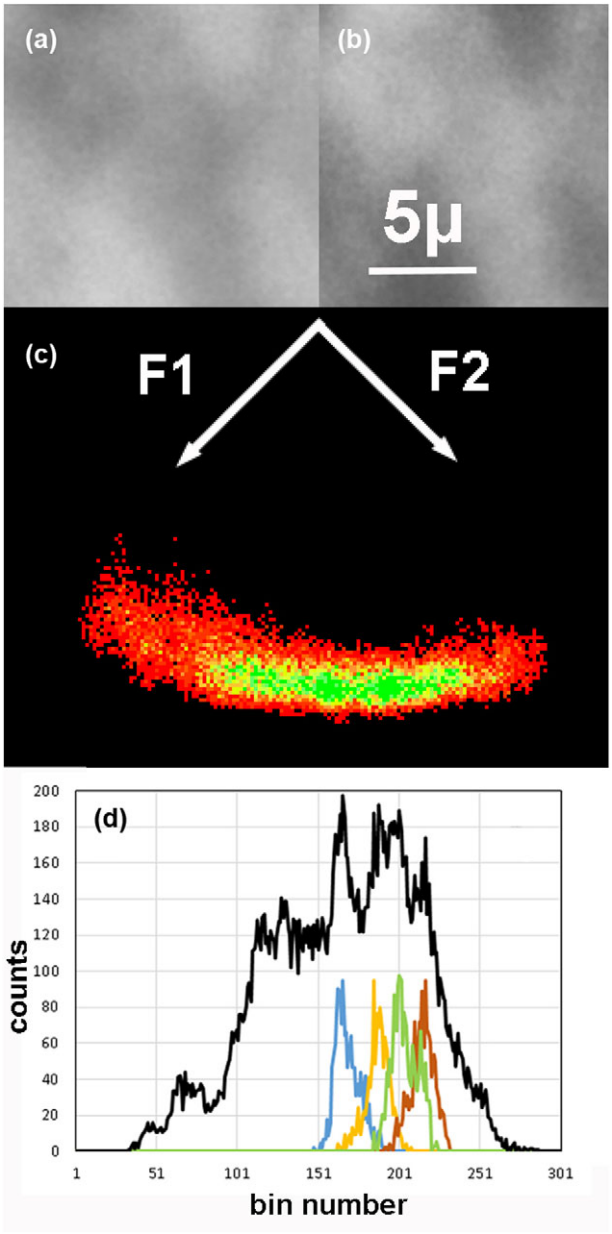

Fig. 13. Image stack data from within the box in the lower left of Figure 11(A). (A) F1 factor image. (B) F2 factor image. (C) Covariance scatter diagram of the F1 and F2 images. (D) Histogram of the scatter diagram in Figure 13(C) along the horizontal direction (black line), histograms from different 2 µm × 2 µm regions in the factor images (coloured lines).

the pattern intensity still further by spatial averaging. After alignment, the image stack can be summed. The summed image is shown in Figure 16(C); the hexagonal pattern has been removed. The contrast of the summed image (Fig. 16C) has also been enhanced by a factor x2.

Figure 16(D) shows the F2 minus F1 image for this image stack. Figure 16(D) has many features that are similar

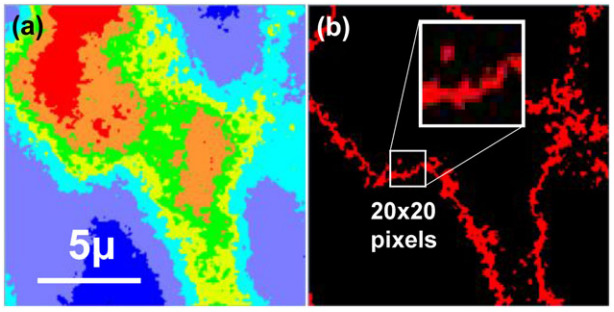

Fig. 14. (A) False colour image from the histogram (Fig. 13D). Red areas are low Al (spectra F2), blue areas are high Al (spectra F1). (B) The 20–80% signal overlap region between the cyan and yellow regions is imaged in red. The 20 × 20 pixel boxes are 1.7 µm × 1.7 µm.

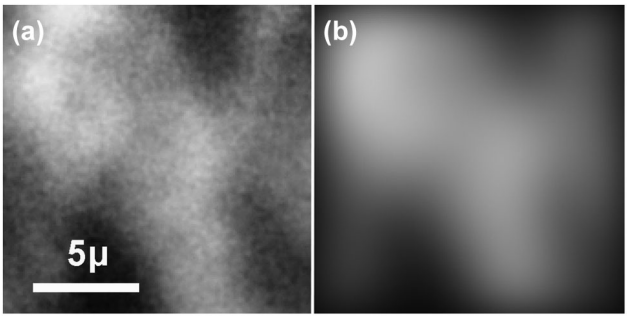

Fig. 15. (A) F2 image minus F1 image (Figs. 13A and B). (B) F1 minus F2 image with a Gaussian blur equivalent to the expected VPPEM spatial resolution of 1.7 µm.

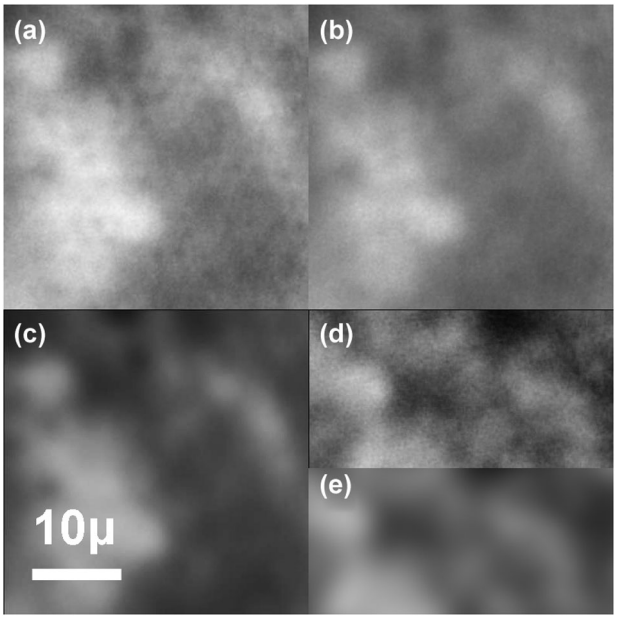

Fig. 16. Cropped image 500 × 500 pixels from the centre of Figure 8. (A) Region showing hexagonal stacking pattern for fibre optical window. (B) Region (A) after FFT filtering. (C) Summed image of the aligned 72.0 to 87.5 eV image stack. (D) F2 minus F1 image (E) F2 minus F1 image with a 1.7 µm Gaussian blur.

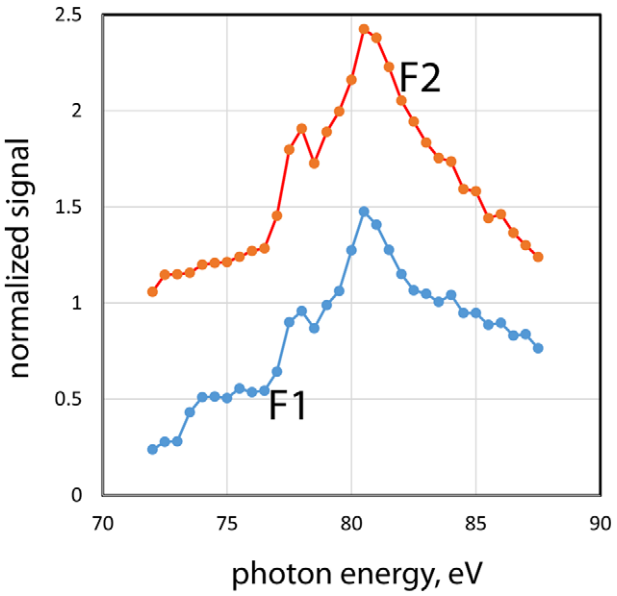

Fig. 17. Factor spectra from a 500 × 500 pixel region at the top of Figure 8. F1 spectrum from an Al-rich region. The Al 2p core absorption peak is at 74.0 eV. F2 spectrum is from a region with low Al 2p core absorption.

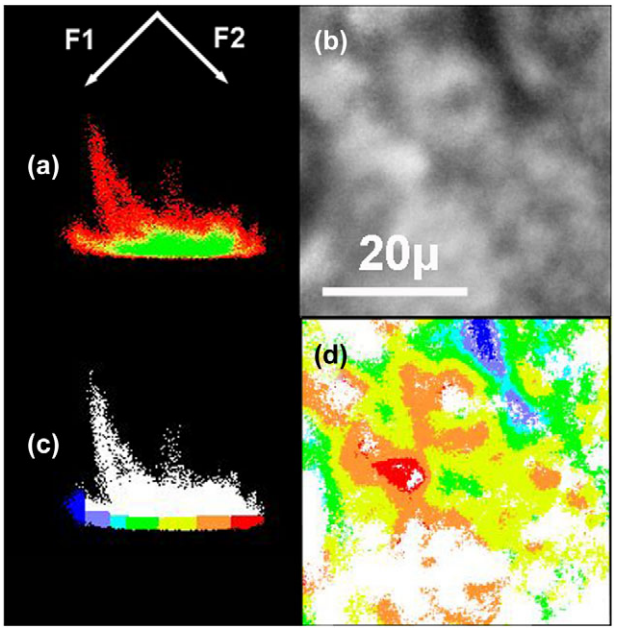

Fig. 18. (A) Rotated F1–F2 scatter diagram based on spectra (Fig. 17). (B) F1 minus F2 image of 500 × 500 pixel region at the top of Figure 8. (C) Rotated F1–F2 scatter diagram coloured to isolate regions along the horizontal axis. (D) False colour image based on the scatter diagram (Fig. 18C).

to the summed image Figure 16(C), but is much sharper. Figure 16(E) is the same image as Figure 16(D) with an additional Gaussian blur equivalent to the expected spatial resolution of the VPPEM, 1.7 μm or 20 pixels.

Figures 17 and 18 are derived from the top 500 × 500 pixel (42.7 μm) region of Figure 8 over the range of 72.0 to 87.5 eV. The two extrema spectra for this region, F1 and F2, are shown in Figure 17. Spectrum F1 (blue) is the high Al spectrum which shows the Al 2p core absorption edge at 74.0 eV, the Al oxide 2p absorption edge at 78.0 eV and the mixed peaks above 78.0 eV.

The low Al spectrum F2 (red) shows a much higher background, little or no Al 2p absorption at 74.0 eV, significant Al oxide with mixed absorption and direct emission peaks at above 78.0 eV. Note that these two spectra are not as extreme as the spectra of Figure 12. The higher background in the low Al regions is evident in the raw images and the summed image (Fig. 16C). The F2 minus F1 images are consistent with the raw images; high Al regions are darker and low Al regions are brighter.

Figure 18 shows data from the 500 × 500 pixel region. The general features of the area can be seen in the F2 minus F1 image in Figure 18(B).

Figure 18(A) shows the 45° rotated scatter diagram of the 500 × 500 pixel area. The majority of the data is along the horizontal direction and the F2 minus F1 image in Figure 18(B) represents the main regions. However, there is significant signal away from the main axis due to a void and other features.

Partitioning the image into a false colour image can be accomplished by using a one-dimensional histogram along the horizontal axis of the scatter diagram Figure 18(A). Because of the presence of the off-axis signal, it is best to concentrate on smaller regions that have contrast change only along the horizontal direction. To isolate the on-axis data, the 500 × 500 pixel scatter diagram of Figure 18(C) is coloured as shown. This produces the false colour image (Fig. 18D). The areas that are not coloured are the off-axis data. In Figure 18(D), the high Al (F1) is coloured blue and the low Al (F2) is coloured red.

The regions of the image that have a simpler histogram along the one axis can be bounded and imaged separately. Two histograms are shown in Figure 19. The histogram in blue is from a 10 μm area covering the blue region at the top of Figure 18(D). The histogram in red is from a 5 μm area near the red region at the centre of Figure 18(D). The red histogram has been scaled up by a factor x4.

The different regions can be imaged by using a hard threshold at the valleys between the signal levels. The resultant false colour images are shown in Figure 20.

The three blue regions (dark blue, light blue, cyan) seen in Figure 20(A) are the three strong peaks on the left of the blue histogram (Fig. 19). Taking the peak positions of the main peaks in the histogram of Figure 20(A) and imaging the 20–80% signal overlap between regions gives the image in Figure 20(B). The 20–80% overlap measured from the peak positions between the dark blue region and the light blue

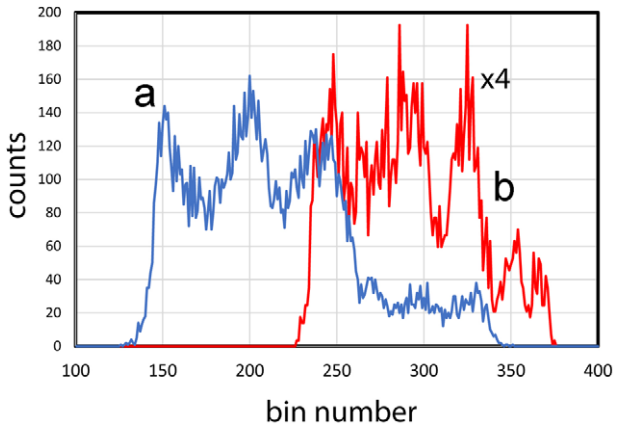

Fig. 19. Histograms from two regions in the image of Figure 18(D). (A) Histogram of 10 μm × 10 μm region covering the blue region at the top of the image. (B) Histogram of a 5 μm × 5 μm region covering the red region at the centre of the image. The red histogram has been multiplied by 4 to scale it to the blue histogram.

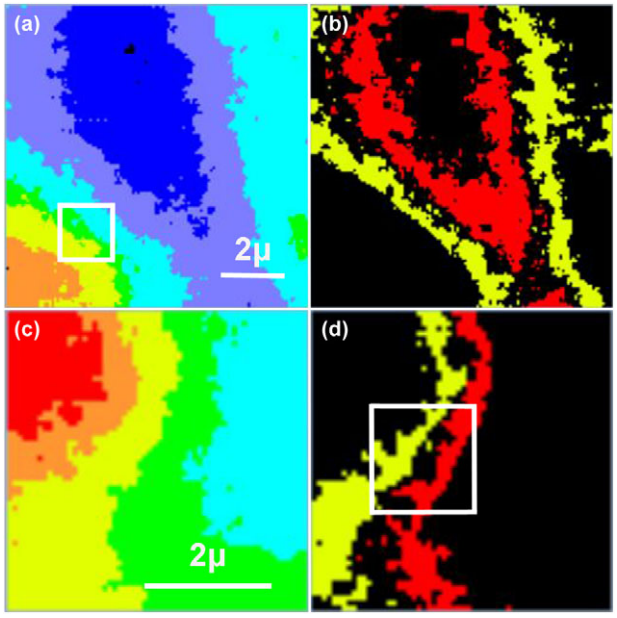

Fig. 20. (A) 10 μm × 10 μm false colour image derived from the blue histogram (Fig. 19A). The six peaks in the histogram are colour coded from left to right, dark blue through orange. (B) Image of 20–80% signal overlaps: red between the dark blue and light blue regions and yellow between the dark blue and cyan regions. (C) 5 μm × 5 μm false colour image derived from the red histogram (Fig. 19B). The six peaks in the histogram are colour coded from right to left, red through cyan. (D) Image of 20–80% signal overlaps: red between the green and yellow regions and yellow between the yellow and orange regions. The white boxes are 1.7 μm × 1.7 μm.

region has been imaged in red in Figure 20(B), and the 20–80% overlap between the light blue region, and the cyan region has been imaged in yellow. The white box in Figure 20(A) shows the expected 1.7 μm (20 pixels) spatial resolution.

Figure 20(C) shows the 5 μm × 5 μm false colour image derived from the red histogram of Figure 19(B). The red region is the low Al region seen in the centre of Figure 18(D) and is the smaller peak on the right of the red histogram in Figure 19(B). The cyan, green and yellow areas are the three strong peaks. The red and yellow areas in Figure 20(D) are the 20–80% overlaps between the green and yellow, and yellow and orange areas respectively. From the shape of the histogram, the region between the cyan and green areas clearly has another feature. Although the peaks for the green and yellow regions are very distinct, the 20 × 20 pixels white box in Figure 20(D) shows the expected 20–80% spatial resolution.

Although none of these measurements are over sharp edges, the boundaries between levels in Figures 20(A) and (C) still show spatial resolution down to a few pixels.

The complexity of the sample response and the lack of resolution in the spectra make the interpretation of the material composition difficult. From Figure 18(C), it can be seen that much of the information in the image does not just rely on the amplitude of the Al 2p core absorption edge. As discussed above, the additional information can come from sample preparation artifacts and ion cleaning, but also from impurity phases such as oxides. However, similar features would be expected in the lower-energy Ca image stack of 51 images as in the Al stack of 41 images. It was not possible to accurately fit the Al and Ca stacks together using the software alignment routine. In fact, in many places, the Al and the Ca signals look very different. However, there are some regions that have small voids with high signal contrast. The centre of these voids can be imaged to a few pixels in both the Ca and Al images allowing us to overlap the images.

Figure 21 is data from a 5 μm region with a small void at the top left-hand side. The Ca signal is from an image stack of 21 images over the range 20.0–30.0 eV covering the Ca 3p core absorption features, the Al signal is from the same 32 images 72.0–87.5 eV used for Figures 17 and 18. The Al false colour image is Figure 21(A), the Ca false colour image Figure 21(B), with the respective F1–F2 histograms Figures 21 (C) and (D).

Figure 21 demonstrates that there is a correspondence between peaks in the histograms derived from Al and Ca image stacks. The correspondence between the small peaks on the left-hand side of the main cluster of peaks is indicated by a line drawn between them. These peaks are imaged in purple in Figures 21(A) and (B). Field distortion and shifts in the image across the field means that an exact one-to-one correspondence is not possible. However, we can make the conclusion that the high spatial resolution phenomenon is present in both images.

Discussion of results

Conventional measurements of spatial resolution across an edge give results that are consistent with the theory of

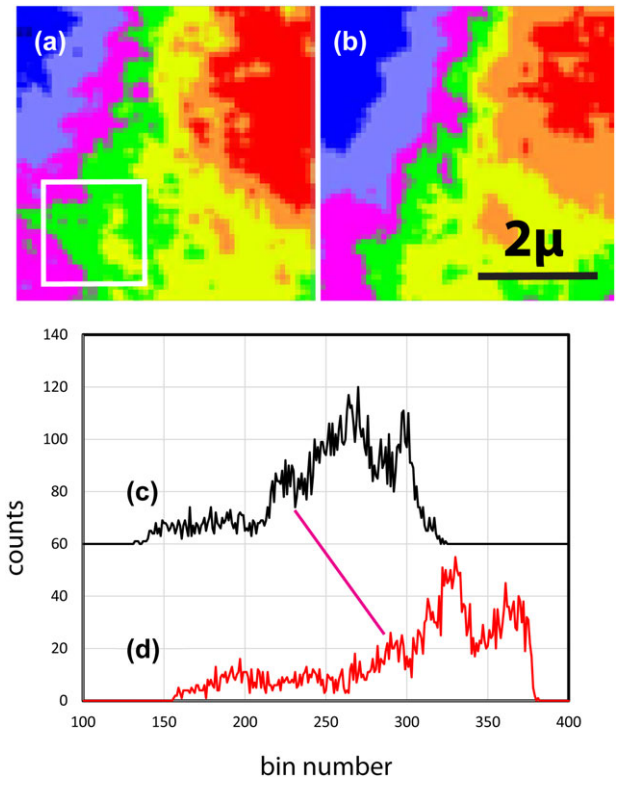

Fig. 21. Comparison of Al 2p and Ca 3p core absorption image stack data. (A) 5 μm × 5 μm false colour image based on the Al image stack histogram C. Areas high in Ca are in red and high in Al in blue. The white box is 1.7 μm × 1.7 μm. (B) 5 μm × 5 μm false colour image based on the Ca image stack histogram D. (C) Histogram of 72.0 to 87.5 eV image stack. (D) Histogram of 20.0 to 30.0 eV image stack. The purple region in both the false colour images 21(A) and (B) corresponds to the peaks indicated by the line between the histograms 21(C) and (D).

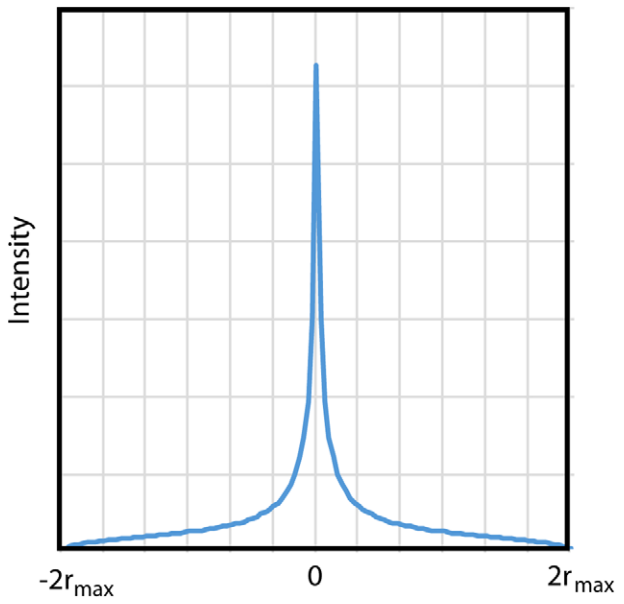

Fig. 22. The point spread function for a magnetic projection lens imaging monochromatic electrons has an aculeate centre with a wide halo out to twice the maximum cyclotron radius, r_{max}.

image formation in magnetic projection microscopes and the VPPEM (Figs. 1 and 11; Beamson *et al.*, 1980, 1981; Kruit & Reed, 1983; Browning, 2014a), whereas the VPPEM images in Figures 14, 20 and 21 are not consistent with this theory. Although the sample is a complex inhomogeneous materials system and not the ideal object for tests of spatial resolution, even so, it is clear that the apparent spatial resolution is much higher than expected and there is very significant high-resolution information in the images. The question is why it appears to be much higher than the full signal edge resolution?

The VPPEM PSF is shown in Figure 22 (Browning, 2014a). The PSF is highly peaked in the centre with wings extending out to twice the maximum cyclotron orbit radius, r_{max}, for the imaging electron energy in the magnetic field at the sample. The maximum cyclotron orbit radius for 1.0 eV electrons in a 1.8 T magnet will be 1.87 μm. There are four radii across the distribution and with 11.7 pixels μm^{-1} the PSF will be 87 pixels across. We can simulate what we would expect to get by convoluting the PSF with a variety of test images. These simulations can be compared with the experimental results. It might be expected that the aculeate central region of the PSF would lead to a high spatial resolution when the background from the diffuse wings are removed (Beamson *et al.*, 1980, 1981). However, this is not the case because the central peak does not contain sufficient signal. The first 2 pixel radius only contains 4.0% of the signal and the experimental results are much sharper. Figure 14(B) shows that 60% of the total signal level can change over 3–4 pixels.

The difference in the spatial resolution at the sample edges and in the region of elemental changes suggests that the spatial resolution is sample-dependent. There is a strong anticorrelation of brightness of the summed image with the Al signal. We expect work function differences across the sample are related to this change in brightness. Work function differences in the 1.0–2.0 V range are seen in the freshly ion-cleaned sample shown in Figure 9.

There are two possible mechanisms related to changes in work function that could give higher spatial resolution. First, the change in work function brings in uncertainty as to what electron energy is being observed and it could be much lower than the nominal value. The energy resolution calculated from the CHA settings is 0.25 eV. The electrons imaged are nominally at 1.0 eV. If there are differences in work function across the sample, then the electron energies could well have a greater range than 0.25 eV. Given the high resolution of the images, the electron energy could be lower. But not as low as 0.1 eV where we would see an extinction of the signal. Taking a midpoint, the calculated edge resolution of 0.5 eV electrons in a 1.8 T field is 1.2 μm. This figure is still over a micrometre

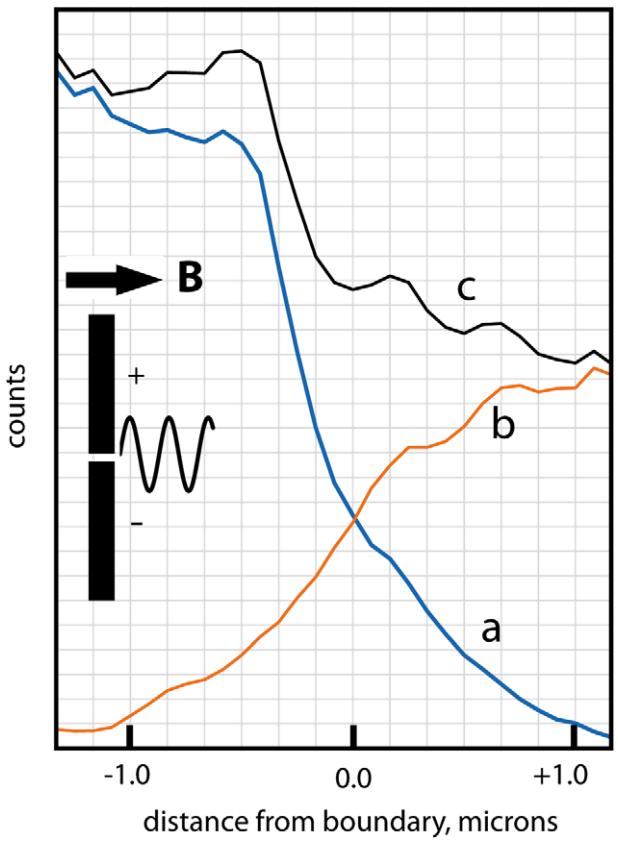

Fig. 23. Monte Carlo calculation of the projected cyclotron orbit distribution away from a potential boundary in a magnetic field for electrons in with average energy of 1.0 eV in a 3.8 T field. Inset is a schematic of the geometry. (A) The projected end point distribution for 0.5 eV electrons emitted from a surface with –0.5 V potential. (B) The projected end point distribution for 1.5 eV electrons emitted from a surface with 0.5 eV potential. (C) The sum of the distributions 23A and B. Trajectories calculated using TriComp software package Field Precision LLC).

and much larger than the spatial resolution suggested by the images. Therefore, the enhanced spatial resolution does not appear be due to measurement uncertainty in the imaging energy.

The second possible explanation is that the changes in work function at compositional boundaries are distorting the low-energy cyclotron orbits. We have carried out a simulation of the possible distortion effects using a Monte Carlo calculation with a finite element electron optical software package (Field Precision LLC, Albuquerque, NM, USA.).

The cyclotron orbits were calculated for a 3.9 T projection field. With the projection magnification in the calculation, this field produces a 1.0 μm cyclotron radius at the detection plane for 1.0 eV electrons. The simulation used 5000 trajectories from the surfaces on each side of a –0.5 to + 0.5 eV step function from –5.0 to 0.0 μm and 0.0 to + 5.0 μm with the positive and negative surface separated by 0.1 μm. The inset of Figure 23 shows the geometry of the simulation. Electrons emitted from the negative surface are emitted at 0.5 eV and from the positive surface at 1.5 eV, for an average electron energy of 1.0 eV. The plot indicated as Figure 23(A) shows the distribution across the boundary for 0.5 eV electron obits leaving the negative surface. It appears that the half height of the distribution is 'pulled' back from the boundary and has a steeper midsection created by the suppression of high emission angle orbits by the neighbouring positive potential. The distribution from the positive potential surface is shown as the plot in Figure 23(B). This is similar to the distribution without a potential difference.

The distribution from the negative surface (Fig. 23A) has been given a greater intensity and when this is summed with the distribution of Figure 23(B), a step is formed. The step from one level to another apparently has high spatial resolution, approximately 0.2 μm, because it is sampling the steeper part of the curve of Figure 23(A). It is this step that would be measured when moving from one region of signal intensity to another. Within the constraints of the finite element model used here, this calculation suggests that the electron optical properties of a realistic potential difference at a boundary will apparently enhance the spatial resolution.

We might speculate that the 'pull back' from the boundary in the distribution of Figure 23(A) could in some circumstances produce a dip in intensity between the two regions. We have looked for these phenomena in the data set represented by Figures 13–15.

We look for a dip in intensity by passing a filter over the F2–F1 factor image data. The filter uses a 3 × 3 pixel kernel. The filter first measures the average noise across the image within the kernel to give a normalization for the variance. The filter then looks at the variance of a single pixel from the average signal in the kernel. A dip in the signal at a pixel can then be detected and imaged. Filtering the F2–F1 image data used for Figure 15(A) exposes a dipped boundary. Figure 24 combines the image of the dipped boundary, in green, with the edge boundary of Figure 18(B), in red.

From Figure 24, it can be seen that the green line, which represents a dip in the intensity, follows the edge boundary from Figure 14(B). The dipped signal is only on one side of the edge boundary, as would be expected if the features were created by 'pulling' the apparent edge boundary.

The presence of a signal dip at the boundary falsifies our estimate of the spatial resolution from the scatter diagram because the change of signal from one cluster to another is not monotonic. However, it should be noted that the dip filter producing the green line in Figure 24 is a single-pixel filter. Although the spatial resolution is not fully defined by our method using cluster peak signals, this measurement still supports the fact that the data have high spatial frequencies that can imaged.

In conclusion, the Monte Carlo calculation of Figure 23 and the F2–F1 filtered image of Figure 24 are suggestive that

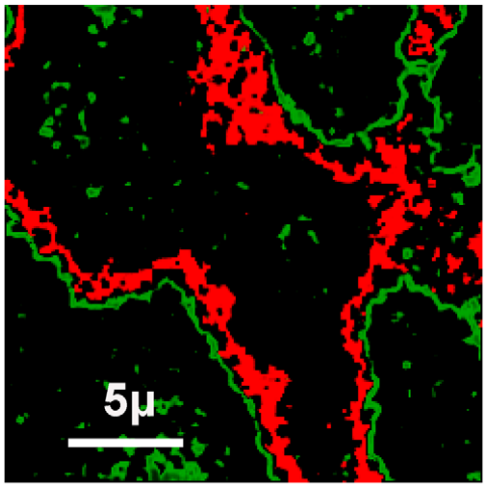

Fig. 24. Data from Figures 14 and 15. Green lines from a 'dip' filter applied to image F2–F1 (Fig. 15A). Red lines are the apparent boundary from Figure 14(B).

surface potential differences are a causative element in the apparently high spatial resolution.

We can compare this result with the effect of surface potentials on the spatial resolution from the PEEM. The sample in the PEEM is the cathode of the electrostatic object lens. Therefore, surface potentials distort the lens field. It has been shown that imaging across a potential boundary with PEEM degrades the spatial resolution with an increase in potential difference (Sangwan *et al.*, 2010). The measured results show good agreement with ray tracing over the modelled geometry. Comparing the PPEM and VPPEM trajectories makes it clear that the near sample behavior is very different for electron trajectories in the two types of microscopes.

Although it is not surprising that surface potential effects should influence VPPEM images, it is remarkable how much information appears in the images. It is not possible from the VPPEM data presented here to fully model the apparent enhancement in spatial resolution and match it to results, as has been done for PEEM. However, the distortion of the near sample obits from a potential difference across a boundary is the right order of magnitude to explain the effects seen.

Conclusion

VPPEM images from chemically inhomogeneous materials have apparent spatial resolutions at compositional boundaries that are significantly higher than expected. A possible explanation of the enhanced resolution is that the low-energy cyclotron orbits are distorted when passing from one area of work function to another. Therefore, the VPPEM image is dependent on the surface field distribution. If this conclusion is correct, there is a possibility of imaging surface chemical distributions at high spatial resolution using the associated surface fields.

Acknowledgements

My thanks to Daniel Fischer of NIST for his support for this work. Thanks are due to Alan Russell of Iowa State University for supplying the very specific samples that we could use. This work has been supported under NIST SBIR contracts SB134113SU637 and SB134114SE0295. Use of the NSLS was supported by the U.S. Department of Energy, Office of Science, Office of Basic Energy Sciences, under Contract No. DE-AC02-98CH10886.

References

Bauer, E. (2012) A brief history of PEEM. *J. Electron Spectrosc.* **185**, 314–322.

Beamson, G., Porter, Q. & Turner D.W. (1980) The collimating and magnifying properties of a superconducting field photoelectron spectrometer. *J. Phys. E Sci. Instrum.* **13**, 64–66.

Beamson, G., Porter, Q. & Turner D.W. (1981) Photoelectron spectromicroscopy. *Nature* **290**, 556–561.

Bianconi, A., Bachrach, R.Z. & Flodstrom, S.A. (1977) Study of the initial oxidation of single-crystal aluminum by inter-atomic Auger yield spectroscopy. *Solid State Commun.* **24**, 539–542.

Browning, R. (1993) Multi-spectral imaging in materials microanalysis. *Surf. Interface Anal.* **20**, 495–505.

Browning, R. (2011) Vector potential photoelectron microscopy. *Rev. Sci. Instrum.* **82**, 103703.

Browning, R. (2014a) Spatial resolution in vector potential photoelectron microscopy. *Rev. Sci. Instrum.* **85**, 033705.

Browning, R. (2014b) NEXAFS/XPS spectra, and information depth using low energy electron spectromicroscopy in a VPPEM. *J. Electron Spectrosc.* **195**, 125–131.

Browning, R. (2015) Vector potential photoelectron microscopy: hyperspectral image processing and super-resolution applied to images of a Ca–Al alloy intermetallic phase distribution. *Surf. Interface Anal.* **47**, 63–76.

Christensen, S.L., Haines, B.M., Lanke, U.D., Paige, M.F. & Urquhart, S.G. (2011) Partial secondary electron-yield NEXAFS spectromicroscopy with an energy filtered X-PEEM. *IBM J. Res. Dev.* **55**(5), 1–6.

Fischer, D.A., Jaye, C., Scammon, K., Sobol, P. & Principe, E.L. (2010) A novel large area imaging NEXAFS spectrometer for combinatorial chemical and structural analysis. *Microsc. Microanal.* **16**(Suppl 2), 380–381.

Horiba, K., Nakamura, Y., Nagamura, N., et al. (2011) Scanning photoelectron microscope for nanoscale three-dimensional spatial-resolved electron spectroscopy for chemical analysis. *Rev. Sci. Instrum.* **82**, 11370.

Joy, D.C. (2002) SMART – a program to measure SEM resolution and imaging performance. *J. Microsc.* **208**, 24–34.

Kim, H. (2011) *Al-Ca and Al-Fe metal-metal composite strength, conductivity, and microstructure relationships*. PhD Thesis, Iowa State University.

Kim, E.J. & Brédas, J.L. (2013) The nature of the aluminum–aluminum oxide interface: a nanoscale picture of the interfacial structure and energy-level alignment. *Org. Electron.* **14**, 569–574.

King, P.L., Borg, Kim, A.C., Yoshikawa, S.A., Pianetta, P. & Lindau, I. (1991) Synchrotron-based imaging with a magnetic projection photoelectron microscope. *Ultramicroscopy* **36**, 117–129.

Kruit, P. & Reed, F.H. (1983) Magnetic field paralleliser for 2π electron-spectrometer and electron-image magnifier. *J. Phys. E Sci. Instrum.* **16**, 313–324.

Martinez, E., Yadav, P., Bouttemy, M., Renault, O., Borowik, L., Bertin, F., Etcheberry, A. & Chabli A. (2013) Scanning Auger microscopy for high lateral and depth elemental sensitivity. *J. Electron Spectrosc.* **191**, 86–91.

Neff, A., Naumov, O., Kuhn, T., Weber, N., Merkel, M., Abel, B., Varga, A. & Siefermann, K.R. (2014) High resolution imaging of a multi-walled carbon nanotube with energy-filtered photoemission electron microscopy. *Am. J. Nano Res. Appl.* **2**, 27–33.

Nepijko, S.A., Sedov, N.N., Schonhense, G., Escher, M., Bao, X. & Huang W. (2000) Resolution deterioration in emission electron microscopy due to object roughness. *Annalen der Physik 9 (Leipzig)* **6**, 441–445.

Pianetta, P., Lindau, I., King, P.L., Keenlyside, M., Knapp, G. & Browning, R. (1989) Core level photoelectron microscopy with synchrotron radiation. *Rev. Sci. Instrum.* **60**, 1686–1689.

Probst, C., Demers, H. & Gauvin, R. (2012) Spatial resolution optimization of backscattered electron images using Monte Carlo simulation. *Microsc. Microanal.* **18**, 628–637.

Sangwan, V.K., Ballarotto, V.W., Siegrist, K. & Williams E.D. (2010) Characterizing voltage contrast in photoelectron microscopy. *J. Microsc.* **238**, 210–217.

Schmidt, Th., Sala, A., Marchetto, H., Umbach, E. & Fruend H.J. (2013) First experimental proof for aberration correction in XPEEM: resolution, transmission enhancement, and limitation by space charge effects. *Ultramicroscopy* **126**, 23–32.

Stohr J. (1992) *NEXAFS Spectroscopy*. Springer Series in Surface Science 25, Springer, Berlin.

Tian, L., Kim, H., Anderson, I. & Russell, A.M. (2013) The microstructure-strength relationship in a deformation processed Al–Ca composite. *Mat. Sci. Eng. A-Struct.* **570**, 106–113.

Uijttewaal, M.A., de Wijs, G.A. & de Groot, R.A. (2006) Generalised coexistence of a low work function and a stable surface: $CaAl_4$ and $BaAuIn_3$. *Surf. Sci.* **600**, 2495–2500.

Wolstenholme, J. (2008) Summary of ISO/TC 201 standard: XXX. ISO18516: 2006 – surface chemical analysis – Auger electron spectroscopy and X-ray photoelectron spectroscopy – determination of lateral resolution. *Surf. Interface Anal.* **40**, 966–968.